Acta Materialia 207 (2021) 116688

Contents lists available at ScienceDirect

Acta Materialia

journal homepage: www.elsevier.com/locate/actamat

Effects of octahedral tilting on the site of substitution of manganese in $CaTiO_3$

Russell A. Maier[a,*], Kevin F. Garrity[a], Andrew Ozarowski[b], Matthew P. Donohue[c,d,1], Giannantonio Cibin[e], Igor Levin[a]

[a] Materials Measurement Laboratory, National Institute of Standards and Technology, Gaithersburg, MD 20899, United States
[b] National High Magnetic Field Laboratory, Florida State University, Tallahassee, Florida 32310, United States
[c] Center for Nanoscale Science and Technology, National Institute of Standards and Technology, Gaithersburg, MD 20899, United States
[d] Maryland NanoCenter, University of Maryland, College Park, MD 20742, United States
[e] Diamond Light Source Ltd., Harwell Science and Innovation Campus, Didcot, OX11 0DE, UK

ARTICLE INFO

Article history:
Received 7 May 2020
Revised 15 January 2021
Accepted 19 January 2021
Available online 22 January 2021

Keywords:
Point defect
Perovskite
EPR
DFT
XAFS

ABSTRACT

Electron paramagnetic resonance (EPR) and X-ray absorption fine structure measurements were combined with first principles calculations to investigate the substitutional behavior of Mn ions in perovskite $CaTiO_3$ ceramics. While transition-metal dopants in perovskite-structured oxides often act as aliovalent defects, Mn in $CaTiO_3$ is amphoteric and concurrently occupies both Ca and Ti sites as Mn^{2+} and Mn^{4+}, respectively. Contrary to the behavior of Mn in $SrTiO_3$ and $BaTiO_3$, which exhibit larger geometric perovskite tolerance factors, in $CaTiO_3$, it is determined that Mn^{2+} prefers A-site substitution. Density functional theory (DFT) calculations provide insight to the unique defect chemistry of Mn-doped $CaTiO_3$ compared to $SrTiO_3$ and $BaTiO_3$, highlighting the role of octahedral rotations which accommodate ionic size mismatch between the larger host and smaller dopant cations on the cuboctahedral sites without significant dopant-ion displacements. Superposition models of the EPR zero-field splitting parameters for multiple types of Mn defect centers were considered based on the structural parameters of DFT calculations, and these results, combined with the EPR, DFT, and X-ray absorption analysis, were used to determine the point defect substitution mechanisms of Mn-$CaTiO_3$.

Published by Elsevier Ltd on behalf of Acta Materialia Inc.

1. Introduction

Complex oxides which crystallize with perovskite-like structures form one of the most versatile classes of inorganic materials because this type of atomic arrangement can accommodate a wide range of chemistries, thus permitting effective compositional control of functional properties [1,2]. For example, relatively small modifications of chemistry can optimize the properties for either ferroelectric [3,4], piezoelectric [5,6], dielectric [7], or ion-conductor [8–12] applications. The functionality of the given perovskite chemistry, as described by the general formula ABO_3, can be predicted using the crystal chemistry rules developed by Pauling and Goldschmidt [13–17]. Deviations of the geometric tolerance factor ($t = \langle A-O\rangle/[\sqrt{2}\langle B-O\rangle]$), which is defined by the ratio of $\langle A-O\rangle$ to $\langle B-O\rangle$ ionic bond lengths, from the ideal value of unity, provide a reliable indicator of the stability of the perovskite structure to lattice distortions. The tolerance factor greater than unity promotes off-centering of B-cations within oxygen octahedra, whereas the opposite case favors cooperative octahedral rotations. These distortions effectively link chemistry to function, providing mechanisms for the compositional tuning of material properties [14,18,19].

Properties of perovskites can also be modified by using dopant species to control the type and concentrations of mobile charge carriers [20,21]. Transition-metal doping mechanisms have been investigated exhaustively in paraelectric $SrTiO_3$ and ferroelectric $BaTiO_3$ and $PbTiO_3$ [20–25]. However, the defect chemistry of the archetype perovskite compound, $CaTiO_3$, has received less attention [26–34]. $CaTiO_3$ differs from the other three compounds by its tolerance factor [1,35] being less than unity, which stabilizes rotations of the [TiO_6] octahedra. This brings up a question about a potential effect of such distortions, which are absent in $SrTiO_3$, $BaTiO_3$, or $PbTiO_3$ [36–38], on the accommodation of substitutional atoms in the host perovskite lattice and on the resulting electronic properties [39] – a topic that has not been previously experimentally explored.

* Corresponding author.
E-mail address: russell.maier@nist.gov (R.A. Maier).
[1] Current address – Seqirus, Holly Springs, NC.

https://doi.org/10.1016/j.actamat.2021.116688
1359-6454/Published by Elsevier Ltd on behalf of Acta Materialia Inc.

Transition-metal species, like Mn, can simultaneously take multiple valence states and lattice site occupations, so the ability to predict and control the site of substitution in a host lattice is challenging [22,40–42]. Here, we combine multi-frequency EPR spectroscopy, X-ray absorption fine structure measurements, and density functional theory (DFT) to investigate the coordination environments of Mn in ceramic $CaTiO_3$. The DFT-based thermodynamic analysis was used to compare the behavior of Mn in $CaTiO_3$ to that in $SrTiO_3$ and $BaTiO_3$, providing insight into the relationship between the site preference for Mn and perovskite crystal chemistry.

2. Material and methods

2.1. Sample synthesis

Ceramic samples of (1-*x*)$CaTiO_3$-*x*Mn with $x = 0.0005$, 0.001, 0.002, 0.005, 0.01, and 0.02 (hereafter, referred to as 0.05Mn, 0.2Mn, 0.5Mn, 1Mn, and 2Mn, respectively) were prepared using standard solid-state synthesis (see Supplementary Information). The final heat-treatment was performed at 1350 °C for 6 hrs in air. The *x*-values were chosen to illuminate any discrepancies in dopant substitutional mechanisms that might be linked to the defect concentration [42].

2.2. Electron paramagnetic resonance

Continuous-wave EPR measurements were conducted at X-band frequencies using a Bruker Biospin (Billerica, MA) ELEXSYS E580[1] spectrometer equipped with a super high Q ER4122-SHQE cavity. The spectra were recorded using the modulation amplitude of 0.5 mT at 100 kHz, which corresponds to ≈1/3 of the narrowest peak-to-peak linewidth, and the incident microwave power of 15 mW at ≈9.7 GHz. High-frequency continuous-wave EPR measurements were conducted in a 17 T transmission spectrometer at the National High Magnetic Field Laboratory (NHMFL). All X-band EPR measurements were performed at room temperature.

2.3. X-ray absorption

Mn *K*-edge (6539 eV) X-ray absorption spectra were measured at the beamline B18 of the Diamond Light Source (Science and Technology Facility Counsel, UK). The measurements were performed on sintered pellets (2Mn) in a fluorescence mode using the 9-element Ge detector. Mn spectra for the reference samples of $SrMn^{4+}O_3$, $YMn^{3+}O_3$, and $Mn^{2+}TiO_3$ have been measured previously at the NIST beamline X23A2 of the National Synchrotron Light Source (Brookhaven National Laboratory). These measurements were performed on powder samples in transmission. All the data were processed and analyzed using the Athena and Artemis modules of the IFFEFIT software package [43]. Scattering phases and amplitudes were calculated using FEFF8 [44]. Theoretical simulations of XANES were performed using the finite-different method implemented in the FDMNES software [45] (see Supplementary Information for details).

2.4. Density functional theory

The DFT [46] calculations were computed with the QUANTUM ESPRESSO [47] code using the GBRV high-throughput ultrasoft pseudopotential library [48]. A plane-wave cutoff of 40 Rydberg and a *k*-point density equivalent to an 8 × 8 × 8 grid in a 5-atom primitive perovskite cell was used with the PBEsol [49] generalized gradient approximation to the exchange-correlation functional. The main results were obtained using DFT+*U* [50] with a Hubbard U parameter of 1 eV on the Mn *d* orbitals to encourage spin-ordering. Additionally, the calculations were performed with a higher U value of 3 eV on both the Mn and Ti d-orbitals; however, the results were qualitatively the same, so the low-U results will be the focus of further discussion. We do not explicitly consider isolated charged defects, but we instead include defect complexes consisting of oxygen vacancies bound to Mn defects. These complexes can allow a transfer of electrons to or from the Mn, resulting in different predicted charge states. We identify the resulting charge states of the Mn by considering the spin and bond lengths, as well as the electronic structure.

To determine low energy geometries, we substituted Mn atoms on either the Ca or Ti sites of the ground state perovskite structure and relaxed using the Broyden–Fletcher–Goldfarb–Shanno (BFGS) algorithm [51]. In addition, to look for symmetry breaking structural distortions caused by defects, we perturbed the atomic positions of each initial atomic configuration randomly multiple times before relaxing, and we keep the lowest energy structure. For structures with an oxygen vacancy, we removed symmetrically-inequivalent oxygen atoms near the defect and followed the same relaxation procedure.

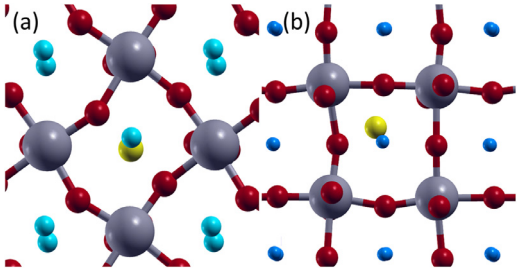

Fig. 1. *a*) Structure of $CaTiO_3$ with Mn on the Ca-sites (i.e. Mn_{Ca}). Ti - grey, O - red, Mn - yellow, and Ca - cyan, and *b*) Structure of $SrTiO_3$ with Mn on the Sr sites (Mn_{Sr}). Sr is shown in dark blue.

3. Results and discusion

3.1. DFT structural analysis

The DFT calculations for the Ca-site substituted Mn indicated that the resulting structure is only slightly distorted from that of pure $CaTiO_3$. The changes are small because of the relatively similar ionic radii of 8-coordinated Ca^{2+} (112 pm) and Mn^{2+} (93 pm) [52] and the large magnitude of the octahedral rotations in $CaTiO_3$ which reduces the ability of Mn to couple to soft modes and distort the structure. After introducing the $Mn_{Ca}^{\times}$ defects (Kröger-Vink notation [53]), the average distance between the Ca-site cation (Ca or Mn) and the four nearest oxygens decreases from 2.36 Å for pure $CaTiO_3$ to an average of 2.18 Å for the doped structure (Table 1) because of enhanced octahedral rotations around the Mn atoms. These rotations in the host lattice allow the structure to accommodate the chemical bonding requirements of the slightly smaller (than Ca) Mn species without significant Mn off-center displacements (Fig. 1a). Such behavior contrasts with Mn-dopants on the Sr site of $SrTiO_3$, shown if Fig. 1b, which display large distortions [40,42]. As expected, Mn ions on the Ca site exist in a Mn^{2+} configuration with a magnetic moment (gS) of $5\mu_B$, and the structure is insulating with a bandgap of 1.57 eV, as compared to 2.43 eV for pure $CaTiO_3$.

[1] The identification of any commercial product or trade name does not imply endorsement or recommendation by the National Institute of Standards and Technology.

Table 1
DFT-derived interatomic distances for the first three coordination shells around Mn on the Ti (Mn_{Ti}) and Ca (Mn_{Ca}) sites, respectively, in the $CaTiO_3$ structure with. The polar θ and azimuthal angles ϕ with respect to the primary Z_{EPR}-axis were calculated from the atomic coordinates in the DFT models.

$Mn^{4+}{}_{Ti}$	**Mn-O**:	R_i	1.903 (× 2)	1.909 (× 2)	1.915 (× 2)						**1st**
		θ_i	2.208,0.9338	2.271, 0.8708	2.051, 1.090						**shell**
		ϕ_i	0.4967, −2.645	2.767, −0.3748	−1.478, 1.663						
	Mn-Ca:	R_i	3.081 (× 2)	3.207 (× 2)	3.293 (× 2)	3.492 (× 2)					**2nd**
	Mn-Ti:	R_i	3.788 (× 2)	3.798 (× 2)	3.799 (× 2)						**3rd**
$Mn^{2+}{}_{Ca}$	**Mn-O**:	R_i	2.070	2.141 (× 2)	2.354	2.739 (× 2)	2.854 (× 2)	2.943	3.135	3.176 (× 2)	**1st**
		θ_i	0.516	2.304, 2.303	1.012	1.029, 1.030	1.881, 1.880	1.863	2.751	1.351, 1.351	**shell**
		ϕ_i	3.141	1.930, −1.930	0	−1.341, 1.341	0.672, −0.672	−3.142	−0.001	−2.334, 2.333	
	Mn-Ti:	R_i	3.177 (× 2)	3.244 (× 2)	3.268 (× 2)	3.419 (× 2)					**2nd**
	Mn-Ca:	R_i	3.712	3.732	3.810 (× 2)	3.877	3.894				**3rd**
$Mn^{2+}{}_{Ti}$	**Mn-O**:	R_i	2.126	2.129	2.140	2.161	2.170	2.179			**1st shell**
		θ_i	2.786	0.348	1.899	1.232	1.353	1.76169			**shell**
		ϕ_i	−2.115	0.876	1.519	−1.649	3.019	−0.145			
	Mn-Ca:	R_i	3.098	3.104	3.226	3.280	3.365	3.387	3.638	3.684	**2nd**
	Mn-Ti:	R_i	3.822	3.869	3.895	3.967	3.989	4.009			**3rd**
$Mn^{2+}{}_{Ti}$-Vac	**Mn-O**:	R_i	1.914	1.933	1.934	1.935	2.054				**1st shell**
		θ_i	1.571	1.564	1.624	1.598	0.093				**shell**
		ϕ_i	2.812	1.238	−0.322	−1.922	−0.937				
	Mn-Ca:	R_i	3.121	3.192	3.275	3.285	3.300	3.399	3.474	3.534	**2nd**
	Mn-Ti:	R_i	3.701	3.773	3.789	3.816	3.820	3.946			**3rd**

*R_i (Å), θ_i and ϕ_i (rad).

Structures calculated for the Ti-site substituted Mn also display only small distortions, with the Mn remaining at the center of the oxygen octahedron. The Mn ions on the Ti-site are in a Mn^{4+} state, with magnetic moment $3\mu_B$, and the structure is again insulating, with a gap of 1.74 eV. To accommodate the slightly smaller size of Mn^{4+}(54 pm) than Ti^{4+}(60.5 pm) [52], the Mn-O distances decrease to an average of 1.91 Å, versus the 1.95 Å Ti-O bonds, and the Mn-O-Ti linkages straighten slightly, to an average of 156°, as compared to the 154° for the Ti-O-Ti angles in $CaTiO_3$.

We also considered defect complexes which consist of an oxygen vacancy and a Mn substitutional defect on the Ca- or Ti-site. We find that none of these defect complexes is thermodynamically relevant for Mn-doped $CaTiO_3$, although the $(Mn''_{Ti} - V_O^{\bullet\bullet})^{\times}$ defect pairs do occur in both the $SrTiO_3$ and $BaTiO_3$ systems at low oxygen partial pressure (see Section 3.4). The lowest-energy $(Mn''_{Ti} - V_O^{\bullet\bullet})^{\times}$ structure in $CaTiO_3$ consists of an oxygen vacancy directly adjacent to the Mn dopant, with only small energy differences between different nearest-neighbor vacancy sites. The complex has one long Mn-O bond of 2.05 Å, with the other four bonds at 1.91–1.93 Å. The resulting complex is metallic with magnetic moment 3.8 μ_B, indicating a mixed valence state. The vacancy is strongly bound to the Mn, with a binding energy of 1.1 eV compared to separated Mn''_{Ti} and oxygen vacancies. This indicates that Mn''_{Ti} will form vacancy complexes if there are any oxygen vacancies available (this is typically the case in perovskites due to the fact that reducing conditions are needed to produce Mn''_{Ti}; and under these conditions, ionic compensation is generally the observed electroneutrality mechanism [20,21]).

In order to consider the possibility of a Mn^{2+} ion appearing at a Ti-site without a neighboring oxygen vacancy, we also performed calculations of Mn_{Ti} with two extra electrons. We find that the extra electrons do bind to the Mn, resulting in a bandgap of 0.37 eV and magnetic moment $5\mu_B$ that indicates a high-spin Mn^{2+} ion. To accommodate the larger size of the Mn^{2+} on the Ti-site, there are large distortions of the crystal structure, with the Mn-O bond lengths increasing to an average of ≈2.15 Å (Table 1), as compared to 1.91 Å for the Mn^{4+}on the same site.

3.2. EPR

3.2.1. X-Band EPR

X-band EPR spectra from polycrystalline Mn-doped $CaTiO_3$ samples are displayed in Fig. 2. For higher Mn concentrations, distances separating the dopant atoms are shortened, which results in significant spin-spin interactions and has the effect of broadening the Lorentzian shape of the EPR linewidth [54,55]. Other than the linewidth and a background broadening term (see Supplemental Information), the resonance of each sample is fit (Easyspin [56]) with identical terms from the simplified effective spin-Hamiltonian:

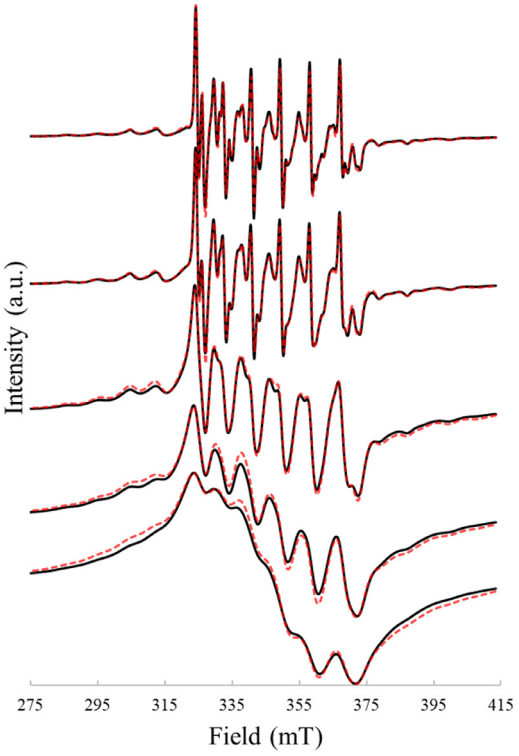

Fig. 2. X-band EPR spectra for $CaTiO_3$, as sintered (*solid black*), with the superimposed fitted signal (dashed-red) for samples (*from top to bottom*) 0.05Mn, 0.2Mn, 0.5Mn, 1Mn, and 2Mn. (For interpretation of the references to colur in this figure legend, the reader is referred to the web version of this article.)

$$\hat{H} = \mu_B B g_{iso} \cdot S + A_{iso} I \cdot S + D \cdot \left[S_z{}^2 - \frac{1}{3} S(S+1) \right] + E \cdot \left(S_x{}^2 - S_y{}^2 \right) \quad (1)$$

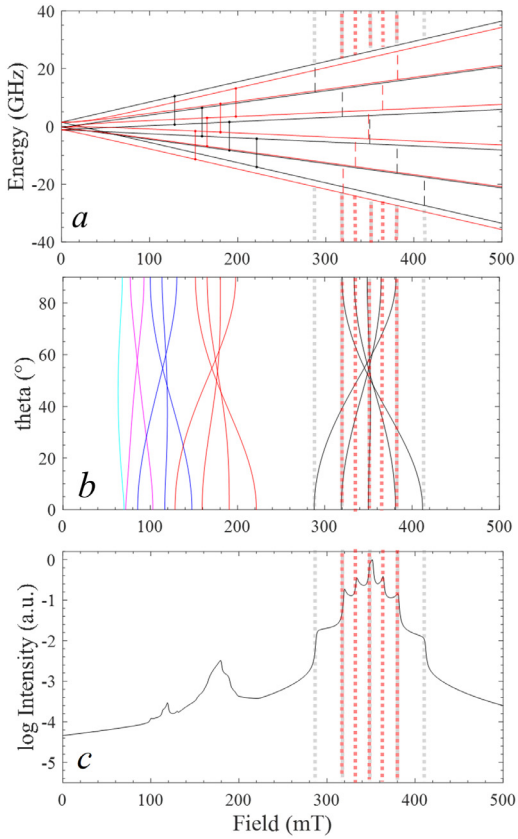

Fig. 3. *a*) Simulated energy level splittings for an $S = 5/2$ ion in a crystal with $D = 435$ MHz and its primary axis oriented at $\theta = 0$ (*black*) and $\theta = \pi/2$ (*red*). The allowed ($M_s \pm 1$) and unallowed ($M_s \pm 2$) transitions are indicated using dotted and solid vertical lines respectively. *b*) The resonance conditions in *a*) rotated from $\theta = 0$ to $\pi/2$ with the transitions $M_s \pm 5$ (*cyan*), $M_s \pm 4$ (*purple*), $M_s \pm 3$ (*blue*), $M_s \pm 2$ (*red*), and $M_s \pm 1$ (*black*). *c*) The absorption response of the spin-Hamiltonian parameters used in *a*) and *b*) averaged over all orientations of θ and ϕ at room temperature to produce the given powder spectrum. (For interpretation of the references to colur in this figure legend, the reader is referred to the web version of this article.)

where μ_B, B, g_{iso}, A_{iso}, I, D, and E is the Bohr magneton, applied external magnetic field, isotropic *g*-factor, isotropic hyperfine interaction constant, the nuclear-spin operator, and the second-rank fine-structure (zero-field splitting) terms respectively. Higher rank fine-structure terms should be included in Eq. (1) for completeness; however, the evaluation of these terms in a polycrystalline sample with hyperfine splitting is non-trivial and the magnitude of these terms are predicted to be negligible in comparison to the second-rank values (see Section 3.2.3).

Mn^{2+} is an $S = 5/2$ ion which implies splitting of its Zeeman energy into $(2S + 1)$ levels having quantized slopes with respect to the applied magnetic field of $M_s = +5/2, +3/2, +1/2, -1/2, -3/2$, and $-5/2$ (Fig. 3a). For simplicity, Fig. 3a-c do not include the hyperfine splitting term A_{iso}. Because the manganese ion, in addition to having unpaired electronic spin is a nuclear isotope with nuclear spin $I = 5/2$, each energy level in Fig. 3a will be split into an additional $(2I+1)$ lines. The center of each pair of hyperfine lines corresponds to the critical points shown in Fig. 3a-c. Mn^{4+} has $S = 3/2$, and the same spin-Hamiltonian (Eq. (1)) as the $S = 5/2$ ion can be used. Typically, Mn^{3+} exhibits D values on the order of 100 GHz and is easily observed in high-field EPR (HFEPR) of concentrated powder samples [57]. However, because of the relatively low sensitivity of HFEPR, detection of Mn^{3+} as a low-concentration dopant is unlikely [58].

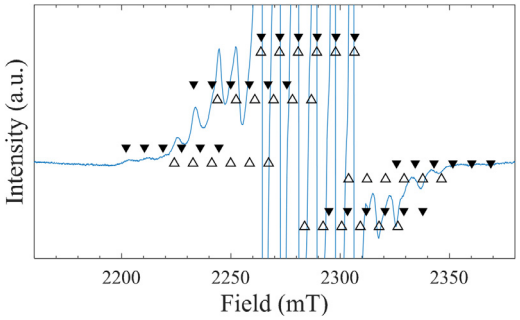

Fig. 4. EPR spectra for the 0.05Mn-doped $CaTiO_3$ sample measured at 64 GHz and 295 K with positions of the best-fit critical points for simulated crystal orientations of $\theta = 0$, $\phi = 0$ (*filled triangles*) and $\theta = \pi/2$, $\phi = 0$ (*open triangles*) with $D = 435$ MHz and $E = -41$ MHz. (For interpretation of the references to colur in this figure legend, the reader is referred to the web version of this article.)

The symmetry of the host Ca^{2+} and Ti^{4+} sites in $CaTiO_3$ is not cubic, so for the Mn ions present on these sites, additional zero-field splitting terms D and E must be present. The ratio E/D is allowed to assume values in the standardized range [59] of $-1/3 < E/D < 0$, in which the lower and upper limits represent purely rhombic and axial fields, respectively [60]. If D is nonzero, the values of the Zeeman energy are shifted along the energy-axis at zero magnetic field by $-8D/3$, $-2D/3$, and $+10D/3$ for the $M_s = \pm 1/2$, $\pm 3/2$, and $\pm 5/2$ doublets respectively (Fig. 3a). For an applied microwave frequency, υ, absorption will occur at an energy level that satisfies the condition $M_{S+1} - M_S = h\upsilon$. The position of the resonance lines for a paramagnetic ion are orientationally dependent, and the D and E terms, are described to first-order approximation using perturbation theory as:

$$B_{M_S \rightarrow M_S - 1} = \frac{h\upsilon}{g_{iso}\beta} - \left(M - \frac{1}{2}\right)\left[D\left(3\cos^2\theta - 1\right) + 3E\sin^2\theta\cos 2\phi\right] \quad (2)$$

where B is the field position of a particular $M_S \rightarrow M_{S-1}$ resonance condition, θ is the angle between the principle axis (Z_{EPR}) and the applied magnetic field, and ϕ is the azimuthal angle. Assuming $E = 0$, all $M_S \rightarrow M_{S-1}$ resonance lines are separated by values of $2D$ for $\theta = 0$ and D for $\theta = \pi/2$ (Fig. 3b). For a polycrystalline sample, because the resonance lines are determined by an integration over the entire range of θ and ϕ, the magnetic field values with the largest $d\theta/dB$ (Fig. 3c) correspond to critical points in the polycrystalline resonance spectrum. The value of D can be estimated from the distance between critical points in a polycrystalline spectrum (Fig. 4).

The first-order values of A_{iso} and g_{iso} are estimated by the separation of the resonance lines of the central sextet as described elsewhere [22]. Using the data in Figs. 2 and 4, initial estimates of the g_{iso}, A_{iso}, D, and E terms are made, and a more accurate determination of the spin-Hamiltonian parameters is achieved with a non-linear least squares refinement [56]. The best fit (red-dash line in Fig. 2, *R*-value of 1.5%) was obtained with values of g_{iso}, A_{iso}, D, and E equal to ≈ 2.001, 239 MHz, 435 MHz, and -40.6 MHz, respectively. A fit of the experimental data using these parameters reveals that the additional $M_s \pm 2$ signals are present (Fig. 5) and the simulation of these "forbidden" transitions also agree well with the fitted spin-Hamiltonian parameters.

3.2.2. High-field EPR

The HFEPR response of a polycrystalline 0.05Mn sample is shown in Fig. 6. Fig. 7a illustrates the theoretical effect of temperature on the absorption spectrum. At higher temperatures, all transitions take place, but close to absolute zero, the lowest levels are

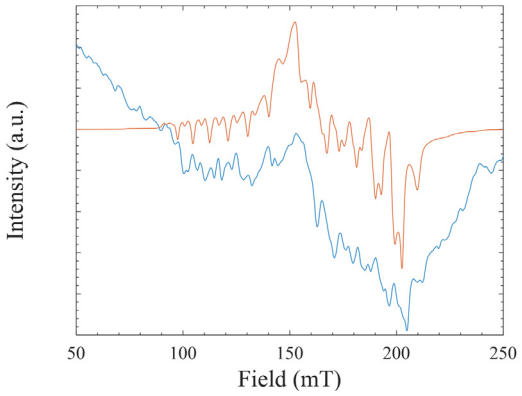

Fig. 5. X-band spectra for the 0.2Mn sample averaged over 50 identical field-sweeps showing the low-intensity resonance of $M_s \pm 2$ transitions (*blue*) and the simulated spectrum (*red*). (For interpretation of the references to colur in this figure legend, the reader is referred to the web version of this article.)

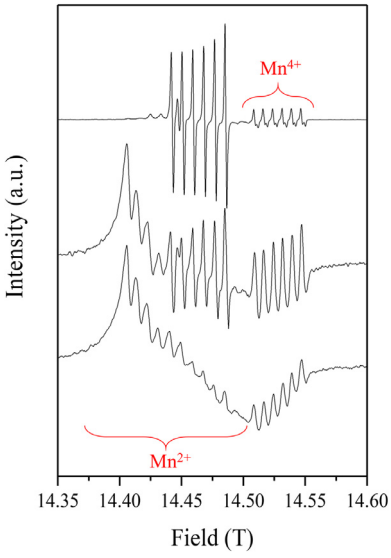

Fig. 6. High-field EPR spectra for the 0.05Mn-doped $CaTiO_3$ samples measured at 405.1 GHz and temperatures of (*from top to bottom*) 50 K, 10 K, and 5 K. (For interpretation of the references to colur in this figure legend, the reader is referred to the web version of this article.)

filled first following Boltzmann statistics. At such low temperatures and with $D > 0$, the high-field $\theta = \pi/2$ transitions occur first between the excited levels, and the weighting of the resonance spectrum is shifted to the low-field transitions (Fig. 7a), while the $\theta = 0$ transitions exhibit the opposite behavior. This effect is observable when the Zeeman energy is comparable to k_bT and thus requires use of high-field EPR at low temperatures. Additionally, if the local symmetry of the coordination environment around a paramagnetic ion is purely rhombic (E= -D/3), the magnitude of the ZFS splitting is the same with opposite temperature dependencies for $\theta = 0$ and $\pi/2$ orientations resulting in a symmetric response for a powder or polycrystalline spectrum at low temperature (Fig. 7b). Experimental observation of the increase in intensity of the lower-field lines (Fig. 6) requires the value of D to be positive and the value of E to be closer to zero than -D/3.

At high field, an additional defect center is observed with $g_{iso} \approx$ 1.995 and $A_{iso} \approx$ 212 MHz (Fig. 6), which are typical parameters for Mn^{4+}[22,61] on the Ti-site. Thus, the high-frequency measurement separates signals that are linked to the Ca-site and Ti-site substituted defect centers, which could not be discerned solely using EPR X-band spectroscopy. As discussed in ref [22], due to the

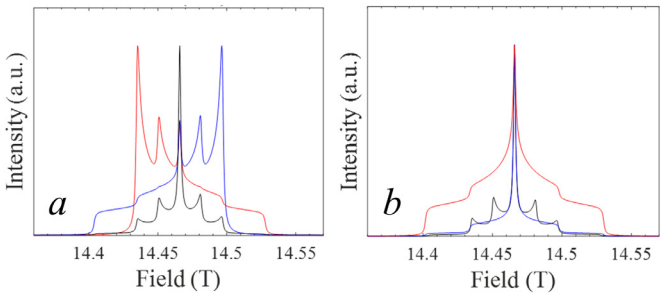

Fig. 7. *a*) Simulated high-field absorption response at 405.1 GHz of a polycrystalline sample with D = 435 MHz at 300 K (*black*), D = 435 MHz at 10 K (*red*), and D = −435 MHz at 10 K (*blue*). *b*) Simulated high-field absorption spectrum at 405.1 GHz of D = 435 MHz at 300 K (*black*), D = 435 MHz and E = -D/3 at 300 K (*blue*), and D = 435 MHz and E = -D/3 at 10 K (*red*). (For interpretation of the references to colur in this figure legend, the reader is referred to the web version of this article.)

charge-transfer process of mid-gap defect states, the simultaneous presence of Mn^{2+} and Mn^{4+} is highly unlikely unless the two ions reside on different lattice sites.

3.2.3. Newman superposition analysis

Newman superposition model (NSM) analysis [62–64] was performed to confirm the assignment of Mn^{2+} to the Ca-site. The size of the hyperfine splitting alone [22,65] is insufficient to determine the dopant site of substitution ($Mn^{\times}_{Ca}$ vs. Mn''_{Ti}). NSM analysis was used to compare the experimental ZFS parameters (D and E) fit from the data in Fig. 2 to the NSM parameters calculated from the atomic coordinates defined by the four DFT models (Table 1).

NSM can be used to determine the exact positions of the nearest-neighbor metal-oxygen bonds surrounding a transition-metal ion. The general equation for the NSM is:

$$b_n^m = \sum_i \bar{b}_n(R_i) K_n^m(\theta_i, \phi_i) \tag{3}$$

where b_2^0 is equivalent to the second-order axial ZFS parameter D, b_2^2 is the rhombic term $3E$, and the fourth-rank ZFS parameters a and F are equivalent to $2b_4^4/5$ and $3(b_4^0\text{-}a/2)$ respectively [66]. The expression for K_n^m is given by the spherical harmonic equations:

$$K_2^0(\theta_i) = \frac{1}{2}\left(3\cos^2\theta_i - 1\right) \tag{4a}$$

$$K_2^2(\theta_i, \phi_i) = \frac{3}{2}\left(\sin^2\theta_i cos2\phi_i\right) \tag{4b}$$

$$K_2^1(\theta_i, \phi_i) = 3(\sin 2\theta_i cos\phi_i) \tag{4c}$$

$$K_2^{-1}(\theta_i, \phi_i) = 3(\sin 2\theta_i sin\phi_i) \tag{4d}$$

$$K_2^{-2}(\theta_i, \phi_i) = \frac{3}{2}\left(\sin^2\theta_i sin2\phi_i\right) \tag{4e}$$

$$K_4^0(\theta_i, \phi_i) = \frac{1}{8}\left(35\cos^4\theta_i - 30\cos^2\theta_i + 3\right) \tag{4f}$$

$$K_4^4(\theta_i, \phi_i) = \frac{35}{8}\sin^4\theta_i cos4\phi_i \tag{4g}$$

where θ and ϕ are the polar and azimuthal angles respectively. The polar angle is defined as the angle between the principal Z_{EPR} axis and the direction of a metal-oxygen bond. The azimuthal angle is the angle between the X_{EPR} axis and the projection of the metal-oxygen bond onto the x-y plane. For high-symmetry defect centers, the principal axis is typically defined as the crystal c-axis [67]. For

lower symmetry centers, as is the case in Mn-doped $CaTiO_3$ with octahedral tilt, the principal Z_{EPR} axis does not necessarily coincide with the crystal axes [68,69]. Several methods can be used to determine an unknown primary EPR axis [70–73]. If coordinates of the ions surrounding a defect center are known (in this case they are provided by DFT calculations), the process of determining the principal axis of a low-symmetry defect center can be simplified by substituting the appropriate R_i, θ_i, and ϕ_i values into Eqs. (3)-4 to construct a full D matrix [74]:

$$D = \frac{1}{6}\begin{pmatrix} -2\left(b_2^0 - b_2^2\right) & 2b_2^{-2} & b_2^1 \\ 2b_2^{-2} & -2\left(b_2^0 + b_2^2\right) & b_2^{-1} \\ b_2^1 & b_2^{-1} & 4b_2^0 \end{pmatrix} \quad (5)$$

Solving this matrix for the eigenvectors returns the diagonalized principal values D_{xx}, D_{yy}, and D_{zz} [69] which are related to the second-order D and E values by the expressions D_{xx}= -D/3 + E, D_{yy}= -D/3-E, and D_{zz}= 2D/3.

The function $\bar{b}_n(R_i)$ includes the term for the paramagnetic ion-oxygen bond lengths, R_i, and is assumed to follow a power law:

$$\bar{b}_n(R_i) = \bar{b}_n(R_o)\left(\frac{R_o}{R_i}\right)^{t_n} \quad (6)$$

$$\bar{b}_n(R_i) = -A\left(\frac{R_o}{R_i}\right)^{n} + B\left(\frac{R_o}{R_i}\right)^{m} \quad (7)$$

where the parameters $\bar{b}_n(R_o)$ and t_n are intrinsic values that are typically calculated from uniaxial strain data [75] and have been successfully used to model $S = 5/2$ ions; the Lennard-Jones variation of this function in Eq. (7) has been used for $S = 3/2$ ions [76,77]. Therefore, if the positions of the paramagnetic defect center along with its nearest-neighbor anion ligands are known, the ZFS parameters can be calculated and compared to experimentally determined values.

To identify the site of substitution of the Mn ion, the experimental ZFS parameters were compared to calculated parameters determined by applying the NSM Eqs. (3)-(7) to four different models: *a*) Mn^{2+} substituted at the Ca-site, *b*) Mn^{2+} substituted at the Ti-site with six nearest neighbor oxygen ligands, *c*) Mn^{2+} substituted at the Ti-site with five nearest neighbor oxygen ligands and one oxygen vacancy, and *d*) Mn^{4+} substituted at the Ti-site. The appropriate intrinsic NSM parameters are $t_2 = 7$, $\bar{b}_2(R_o) = -0.05$ cm^{-1}, $t_4 = 10$, and $\bar{b}_4(R_o) = 2.72 \times 10^{-4}$ cm^{-1} for Mn^{2+} [78] and $A = -11.1$ cm^{-1}, $B = -8.48$ cm^{-1}, $n = 10$, and $m = 13$ for Mn^{4+} [76].

The intrinsic superposition parameters $\bar{b}_n(R_o)$ and t_n have not been calculated for Mn-doped $CaTiO_3$. However, these parameters can be adopted from a model host system as long as it has bond lengths and coordination numbers similar to those in the system of interest [79–81]. Superposition parameters for Mn^{2+} and Mn^{4+} in octahedral coordination are available from literature, but parameters for Mn^{2+} on a dodecahedral site are not. From Eqs. (3) and 6 it is observed that the intrinsic parameters don't factor into the superposition calculation of the expression E/D. By modeling E/D, the ambiguity of the intrinsic parameters is avoided. The data in Fig. 8 were calculated using a three-parameter NSM model. The initial bond lengths between the Mn-dopant and its oxygen ligands as well as polar and azimuthal angles were taken from DFT calculations (Table 1). The Mn-ion was allowed off-center displacements of ±10 pm in *x*, *y*, and *z*-directions. For each displacement, the D-matrix in Eq. (5) was constructed, the principal D and E values were calculated, and this process was repeated for a total of 10^6 displacements. The experimental E/D value of −0.093 is close to the value calculated for Ca-site substitution of Mn^{2+}, and the exact experimental value is achieved with small 1 pm displacements of the ion from its DFT predicted position (Fig. 8). Ti-site substitution of Mn^{2+} results in a defect center with high rhombic character ($E/D = -0.25$) for the case of octahedral coordination and a defect center with high axial character ($E/D = -0.034$) for the 5-fold-coordinated Mn^{2+} with a nearest neighbor oxygen vacancy. The R_i, θ_i, and ϕ_i values for the four modeled defect centers with zero displacement and oriented along the principal Z_{EPR} axis are given in Table 1. The ratios a/D and F/D for each sample were also calculated to give an estimation of the scale of the fourth-order parameters with respect to the second-order values. For the A-site Mn^{2+} a/D=-1 × 10^{-3} and F/D = 8 × 10^{-3}, whereas for the Mn^{2+} B-site substitution a/D=-3 × 10^{-2} and F/D = 2 × 10^{-2}. Thus, for the Ca-site substitution, the effects of fourth-order splitting are expected to be small compared to the effects of the second-order parameters.

For the Mn^{4+} B-site substituted model, suitable superposition constants are available from Mn^{4+}-doped $BaTiO_3$ crystals [76]. Using these values, the Z_{EPR} aligned values D and E were calculated as −4070 and 1010 MHz respectively. The high-field EPR data in Fig. 6 shows a single sextet for the Mn^{4+} defect center; however, the calculated NSM values of D and E suggests there should be large splitting resulting in additional features. The resonance lines as a function of rotation are plotted in Fig. 9 for the calculated ZFS values at 9.8 and 400 GHz. For the low-field simulation, the resonance lines are widely dispersed by rotation resulting in broad, low-intensity signals in the field-swept scan of a powder sample. This result can explain the absence of any Mn^{4+} signals in the X-band data in Fig. 2. Conversely, the high-field simulation in Fig. 9 reveals small orientational dependence of the simulated Mn^{4+} signals resulting in a well-defined sextet. Without additional experimental (i.e. single crystal) information concerning the Mn^{4+} features, an exact measurement of the ZFS values cannot be reported. Additional resonance broadening resulting from D-strain and likely g-anisotropy complicates the powder spectra. Multi-frequency measurements were performed to confirm that the distance between the two features labeled Mn^{2+} and Mn^{4+} in Fig. 5 scales with frequency, which confirms that these two sextets belong to separate defect centers with non-equivalent g-factor values. This frequency scaling along with the small hyperfine splitting value and NSM calculated D and E parameters provides significant evidence that the defect center in question is Ti-site substituted Mn^{4+}.

3.3. X-ray absorption

3.3.1. XANES

The oxidation state of Mn can be assessed by a comparison of the X-ray absorption near edge structure (XANES) for the Mn K-edge as measured for Mn in $CaTiO_3$ and in the reference samples $Mn^{2+}TiO_3$, $YMn^{3+}O_3$, and $SrMn^{4+}O_3$. Previous studies of the Mn K-edge XANES in a large number of manganates indicated that the position of the main edge provides a reliable fingerprint of the Mn valence. Both visual examination of the spectra in Fig. 10 and linear combination fits using the reference spectra suggests a concentrated mixture of Mn^{2+} (dominant) and Mn^{4+} (and/or Mn^{3+}) in the $CaTiO_3$ sample [22,82]. The presence of the higher-valence Mn appears to be necessary to reproduce the feature at ≈8.7 eV above the absorption edge. As noted previously, the accuracy of the fractions of these species obtained from such analyses is compromised by the relatively significant discrepancies between the target and fitted signals which arise presumably because the coordination of Mn in all the non-perovskite reference structures differs from that in $CaTiO_3$. Simulations of XANES for the DFT-derived models (Supplementary Information) support the assessments from the comparison of the experimental and reference spectra, providing further indication of the presence of Mn on both Ca- and Ti-sites.

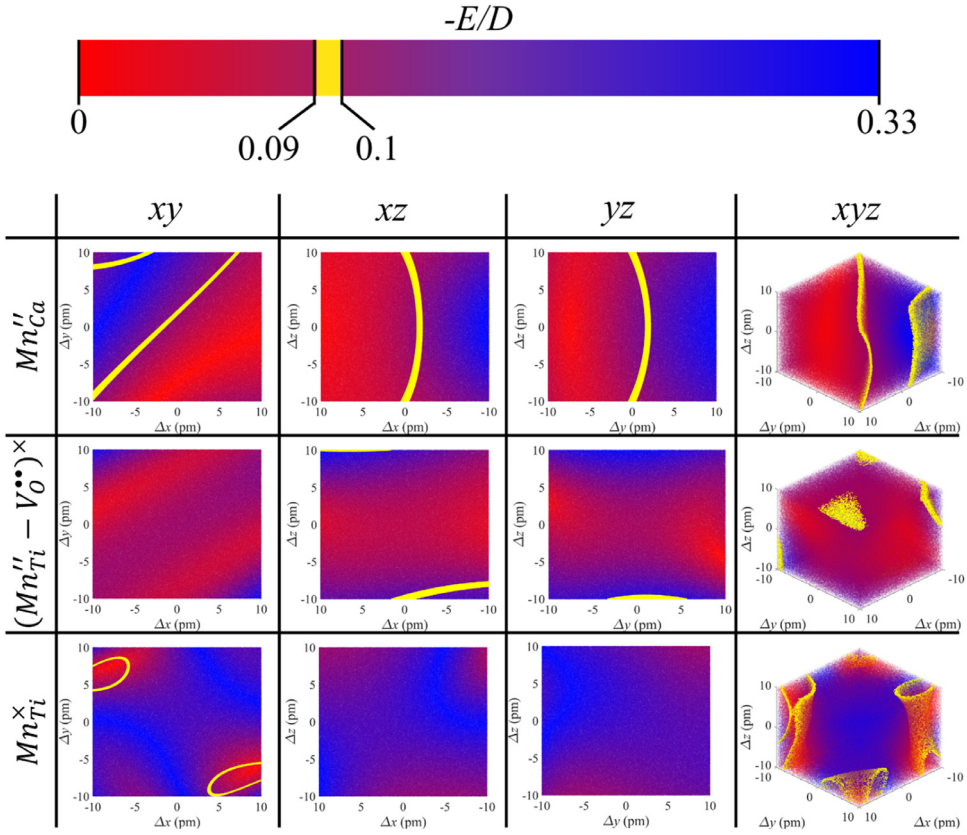

Fig 8. Three-parameter Newman superposition model analysis of the Mn-ion with substitution *top-row*) Mn^{2+} onto the Ca-site, *middle-row*) Mn^{2+} onto the Ti-site with a nearest neighbor oxygen vacancy, and *bottom-row*) Mn^{2+} onto the Ti-site. The superposition model was calculated for Mn-displacements along the *x*, *y*, and *z* axes, with the columns from *left-to-right* corresponding to the *xy*, *xz*, and *yz* planes through the origin of the 3D plot to the *right*. The value *E/D* was calculated for each Mn-displacement with *red* corresponding to an axial center and *blue* a rhombic defect center with a yellow region of $-0.09<E/D<-0.1$ corresponding to the experimentally measured ratio of second order ZFS values.

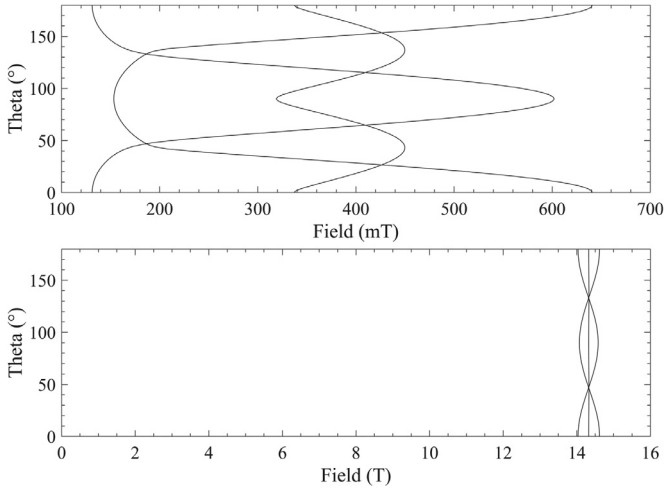

Fig. 9. The simulated rotational dependence of the $M_s \pm 1$ transitions (hyperfine transitions removed) for Mn^{4+} with g_{iso}, *D* and *E* values of 1.995, −4070 MHz and 1010 MHz respectively for microwave frequencies of *top*) 9.8 GHz and *bottom*) 400 GHz.

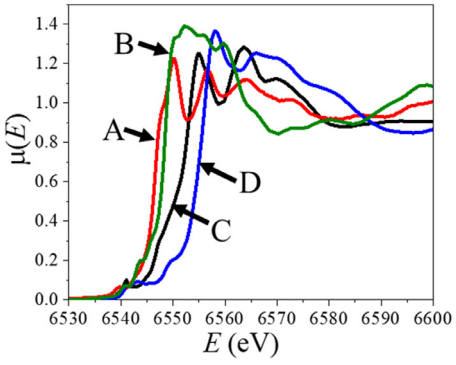

Fig. 10. XANES portions of the Mn K-edge spectra for Mn in $CaTiO_3$ (A, *red*), $Mn^{2+}TiO_3$ (B, *green*), $YMn^{3+}O_3$ (C, *black*), and $SrMn^{4+}O_3$ (D, *blue*). A comparison indicates that Mn in the $CaTiO_3$ sample exhibits a mixed oxidation state with Mn^{2+} being dominant but Mn^{4+} and possibly Mn^{3+} present in significant concentrations. The presence of higher-valence Mn is considered necessary to account for the peak at ≈8.7 eV above the main absorption edge. (For interpretation of the references to color in this figure legend, the reader is referred to the web version of this article.)

3.3.2. EXAFS

Given the mixed oxidation state of Mn inferred from the XANES data, we considered two structural models. In the first model, Mn occupied the octahedral sites regardless of the oxidation state. Since Mn^{2+} is significantly larger than Mn^{4+} or Mn^{3+}, the presence of Mn^{2+} and Mn^{4+}/Mn^{3+}, implies a mixture of octahedra with distinct Mn-O distances. As previously determined for Mn in $SrTiO_3$ [42], the Mn^{3+} coordination environment yields average distances relatively close to those for Mn^{4+}; therefore, these two species are difficult to distinguish from EXAFS of mixed-state samples such as encountered in the present case, although EXAFS simulations (Supplementary information) favor Mn^{2+} on the Ca-sites based on the appearance of the feature at ≈3 Å. Therefore, we assumed a binary mixture of the larger (Mn^{2+}-centered) and smaller (Mn^{4+}-

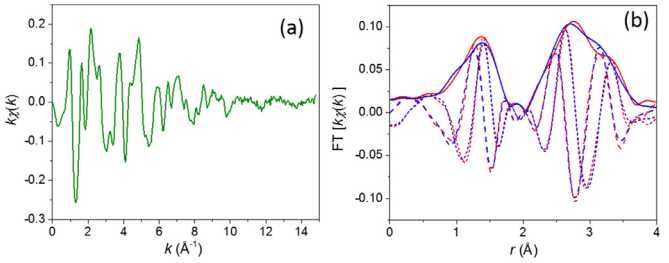

Fig. 11. *a*) Experimental Mn K-edge EXAFS for 2 mol% Mn in $CaTiO_3$, and *b*) Experimental (*red*) and calculated (*blue*) Fourier transform (FT) of the EXAFS signal in *a*). The *k*-range used in the FT was from k_{min}=2.76 Å^{-1} to k_{max}=11.38 Å^{-1}. The fitting range in the *r*-space was from 1 Å to 4 Å. While the data contain a significant signal out to 10 Å, a model required to fit it beyond the first several coordination shells would require too many parameters to be tractable. The modulus, real, and imaginary parts of the FT are indicated using solid, dashed, and short-dashed lines, respectively. The calculated signal corresponds to the mixed-site model described in the text and in Table 2. The *R*-value for the fit is 1.4%. (For interpretation of the references to colur in this figure legend, the reader is referred to the web version of this article.)

Table 2
Parameters of the Mn coordination environment in $CaTiO_3$, as obtained by fitting the EXAFS data (*N* – coordination numbers, *R* – interatomic distances, σ^2 – Debye-Waller factors). Numbers in parenthesis represent a single standard deviation as calculated by the Artemis module of the IFEFFIT package. The refined Ca/Ti site ratio is 2.3(3). The parameters indicated by the asterisk were kept fixed during the fit. The Mn_{Ti}-Ti and Mn_{Ca}-Ca distances were constrained to be equal. The refined value of ΔE_0 was ≈−1.7 eV relative to the main maximum of the 1st derivative of the absorption signal.

Site	Shell	N	R (Å)	σ^2(Å^2)
Mn_{Ti}	Mn-O	6	1.91*	0.005*
	Mn-Ca	2	3.15*	0.006*
	Mn-Ca	4	3.3*	0.012*
	Mn-Ca	2	3.5*	0.012*
	Mn-Ti	6	3.8(1)	0.015(15)
Mn_{Ca}	Mn-O	4	2.25(6)	0.019(8)
		5	2.62(9)	0.018(14)
	Mn-Ti	8	3.21(6)	0.022(6)
	Mn-Ca	6	3.8(1)	0.013(4)

centered) octahedra. In the second model, Mn was present on both cuboctahedral and octahedral sites. In both scenarios, treating all the distances and their associated Debye-Waller factors as variables would lead to overfitting. Previously, while performing a similar analysis for the mixed-valence Mn in $SrTiO_3$, this problem was addressed by fixing the parameters of the coordination environment of Mn_{Ti} at their values determined from the EXAFS fitting for a sample that contained exclusively Mn^{4+} in octahedral coordination. However, in the present case, such samples with single-site substitution were unavailable. Therefore, we adopted several structural characteristics from the DFT results.

First, we used our DFT models to simulate the corresponding EXAFS signals, with simplistic assumptions made about D-W factors (see Supplementary Information for details). A linear 2:1 combination of signals for the Ca-site and Ti-site (Mn^{4+}) models reproduced the overall character of the experimental spectrum. For fitting the EXAFS signal, the DFT models were parameterized at a higher level to minimize the number of parameters. Our DFT-derived distances (Table 1) for the octahedral Mn are close to those established for the Mn^{4+} ions in $SrTiO_3$. Given the rigidity of the [MnO_6] octahedron, we assumed that these theoretical distances adequately represent those associated with Mn^{4+} in $CaTiO_3$. Thus, in both of our EXAFS models, the coordination environment of the octahedral Mn^{4+} was described following the DFT predictions (Table 1). The Mn-O distance was set at 1.91 Å and kept fixed during fitting. The D-W factor ($\sigma^2_{Mn\text{-}O}$) for the Mn-O bond length was fixed at 0.005 Å^2, as observed for Mn in $SrTiO_3$. The Mn_{Ti}-Ca coordination shell was represented using three distances of 3.15 Å (× 2) 3.3 Å (× 4), and 3.5 Å (× 2) which were selected to approximate the DFT predictions and also kept fixed during the fit; the finer splitting of the Mn_{Ti}-Ca distances was assumed to be accounted for by the D-W factors, which were set at a reasonable value of 0.01 Å^2. The only parameters allowed to vary were the Mn-Ti distance and its D-W factor (these parameters were left free as a test for the rest of the Mn^{4+} model). The parameters for the multiple-scattering paths of a photoelectron were expressed in terms of those for the Mn-O and Mn-Ti nearest-neighbor distances and their corresponding D-W factors (see Supplementary Information). Changes in the Mn-O-Ti angles associated with octahedra rotations were assumed to be absorbed by the D-W factors. The only non-structural variable included in the fit was the energy shift ΔE_0; a single value of ΔE_0 was used for Mn in the Ca- and Ti-site coordination, as justified by the previous work [39]. The amplitude-reduction factor S_0^2 was fixed at a realistic value of 0.9.

For the model with the two types of [MnO_6] octahedra, the coordination environment for the Ti-site Mn^{2+} was described similarly to that of Mn^{4+} using single Mn-O and Mn-Ti distances, and three Mn-Ca distances (model with a single Mn-Ca distance was tried as well); each chemically distinct coordination shell was assigned a single D-W factor. All these parameters were treated as variables. The starting values for the interatomic distances were assumed from the results of the DFT calculations (Table 1), which were also used for assessing the soundness of the refined structure. The distances and D-W factors for the photoelectron multiple-scattering paths were parameterized like those for the octahedral Mn^{4+} model (Supplementary Information).

In the model with the mixed Ca- and Ti-site Mn occupancy, the Ca-site coordination environment for Mn was approximated using two Mn-O distances having multiplicities of × 4 and × 5 suggested by the DFT calculations. The cation-cation coordination shells were represented using single Mn-Ti (× 8) and Mn-Ca (× 8) distances, each assigned its D-W factor. Only the single-scattering Mn-O, Mn-Ti, and Mn-Ca paths were included in the fit. A ratio of the Ca- to Ti-site Mn species was treated as a variable. If refined independently, the Mn_{Ca}-Ca and Mn_{Ti}-Ti distances were strongly correlated and, therefore, constrained to be equal, in line with the theoretical predictions (Table 1).

The total number of variables for the EXAFS fit using either model was 10 for the 15 independent points estimated using the Nyquist criterion for the *k*- and *R*-ranges included in the fit (Fig. 11). Both models produced fits of comparable quality. However, refinements of the purely octahedral model consistently returned unphysical values of the Mn-Ca and Mn-Ti distances, which correspond to the 2nd and 3rd coordination shells for the assumed Ti-site Mn^{2+} coordination. The distances for the 2nd shell were significantly longer than those for the 3rd. Attempts to constrain these and other parameters either did not affect the outcome of the fit or resulted in the significantly inferior agreement factors. In contrast, for the mixed-site model (Fig. 11, Table 2), the refined characteristics of the Mn_{Ca} coordination were all meaningful and in agreement with those predicted by the DFT calculations. Therefore, we selected this model with Mn present on both Ca- and Ti-sites as providing an adequate description of the Mn coordination in the sample.

The ratio Mn_{Ca}/Mn_{Ti} of 2.3(3) obtained from the EXAFS fits is consistent with the qualitative inferences about the Mn^{2+} versus Mn^{4+}/Mn^{3+} concentrations from the XANES, thus supporting the partitioning of Mn^{2+} and Mn^{4+}/Mn^{3+} species into the Ca- and Ti-sites, respectively. The Mn^{3+} coordination environment, as previously determined for Mn in $SrTiO_3$ [42], yields average distances

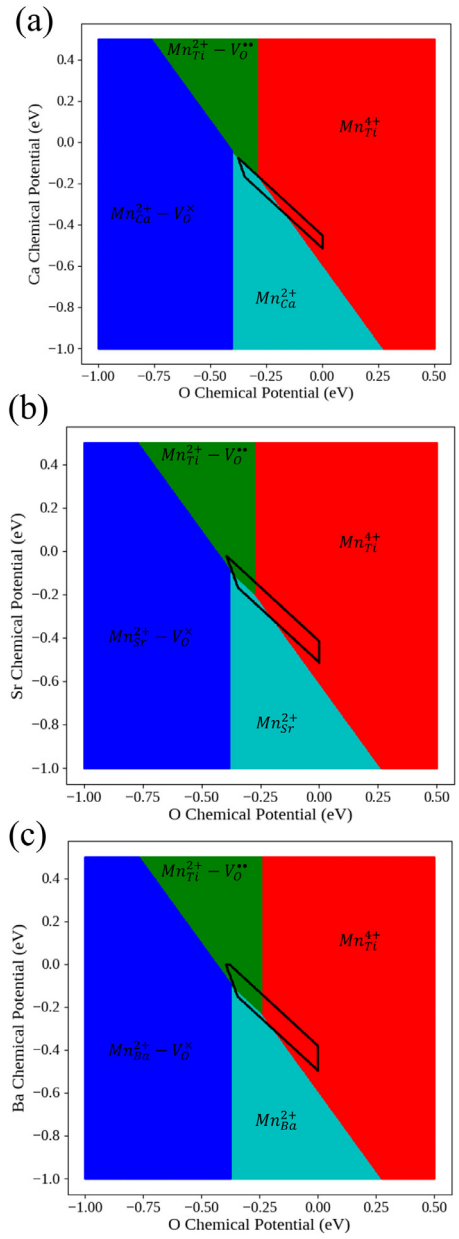

Fig. 12. Phase diagrams of Mn-doped *a*) $CaTiO_3$, *b*) $SrTiO_3$, *c*) $BaTiO_3$. Solid regions indicate structures with Mn-defects: (*red*) $Mn_{Ti}^{\times}$, (*cyan*) is $Mn_{(Ca/Sr/Ba)}^{\times}$, (*green*) is the $(Mn_{Ti}^{''}\text{-}V_O^{\bullet\bullet})$ defect complex, and dark (*blue*) is the $(Mn_{(Ca/Sr/Ba)}^{\times}\text{-}V_O^{\times})$ defect complex substitution. The black regions indicate the thermodynamically stable region of the given perovskite phase. (For interpretation of the references to colur in this figure legend, the reader is referred to the web version of this article.)

relatively close to those for Mn^{4+}; therefore, these two species are difficult to distinguish from EXAFS of mixed-state samples.

3.4. DFT thermodynamic analysis

A first-principles thermodynamic analysis [83] (see Supplement Information for details) of Mn dopants in $CaTiO_3$, $SrTiO_3$, and $BaTiO_3$ was conducted to confirm that the calculations can also reproduce previously published experimental results for Mn-doped $SrTiO_3$ and $BaTiO_3$ [22,84]. The resulting phase diagrams in the chemical-potential space are presented in Fig. 12. In these diagrams, differently colored regions correspond to the stability domains of the four types of defects that can result from the Mn substitution. The trapezoidal region outlined by the black line near the center of each diagram indicates the stable region of the corresponding perovskite phase; that is, only those defects that are stable within these trapezoidal regions can be present in a given perovskite system. The preferred defect depends on the chemical potentials, which are fixed by the experimental synthesis conditions.

Table 3
Site of substitution for Mn predicted from crystal chemistry.

	BVS	GT	Site	Ref
$CaTiO_3$	0.38	0.56	A-site	this study
$SrTiO_3$	0.80	1.45	Mixed	[22,41,42]
$BaTiO_3$	1.17	2.82	B-Site	[84]

The calculations for the bond valence sum (BVS) and Goldschmidt tolerance factor (GT) ratios are described in detail in the supplemental information. The BVS value is the ratio of BVS for A-site versus B-site substitution of Mn^{2+} and Mn^{4+}, respectively. The GT factor is a similar ratio of A- versus B-site substitution of Mn. For each of these ratios, a value less the unity predicts A-site substitution while the opposite relation predicts B-site occupancy. The references describe experimental studies of assignment of the Mn-substitution.

Typically, synthesis and annealing of complex oxides are performed at high temperatures under slightly reducing conditions, which correspond to relatively low values of the oxygen chemical potential. The phase diagram for $CaTiO_3$ in Fig. 12a indicates that both $Mn_{Ca}^{\times}$ and $Mn_{Ti}^{\times}$ defects are possible, with the $Mn_{Ca}^{\times}$ state being dominant for low values of the oxygen chemical potential, which makes it the most probable in practical samples. For $SrTiO_3$ (Fig. 12b), the overall picture is similar, but in the relevant chemical-potential range, the $Mn_{Sr}^{\times}$ defects are expected to coexist with both $Mn_{Ti}^{\times}$ and the $(Mn_{Ti}^{2+} - V_O^{\bullet\bullet})^{\times}$ oxygen-vacancy defect complex. This is consistent with previous experimental work [21,22,41,85] which showed that depending on synthesis conditions (Sr/Ti stoichiometry), Mn resides on either the Sr or Ti-sites and, while on the Ti-site, it can acquire either the 4+ or the 2+ state (depending on the pO_2 during synthesis). Finally, for the $BaTiO_3$ case (Fig. 12c), the $Mn_{Ba}^{\times}$ state is even less favored, being stable only over a very narrow range of conditions. Indeed, substitution of Mn onto the Ba site in $BaTiO_3$ has never been experimentally observed. The overall picture supports a simplistic hypothesis that the smaller cuboctahedral cages in $CaTiO_3$ facilitate Mn substitution on the Ca-sites as Mn^{2+}, while the relatively large Ba-site cages in $BaTiO_3$ favor Mn^{4+} on the Ti-site, as has been also experimentally verified by EPR analysis [84]. For $SrTiO_3$, which represents an intermediate case, the site of substitution is variable and can be controlled by tuning the chemical potential of Sr via the Sr/Ti ratio [22]. The EPR responses for 0.05Mn samples annealed under reducing and oxidizing conditions (Supplementary Information) suggest reduction of the B-site Mn^{4+} ion but provide no evidence of B-site Mn^{2+} or Mn^{2+}-related defect complexes that are typically observed in the cases of Mn-doped $SrTiO_3$ or $BaTiO_3$. Reduction of B-site substituted Mn^{4+} can create the presence of nearest-neighbor oxygen vacancy associated defect complexes, $(Mn_{Ti}^{2+} - V_O^{\bullet\bullet})^{\times}$, with second order ZFS values typically on the order of 10^4 MHz or greater. These large ZFS values are responsible for a distinct resonance feature at $g_{iso} \approx 6$ at X-band [22,42,84,86,87], but no evidence of this defect complex was observed in $CaTiO_3$.

3.5. Crystal chemistry

The thermodynamic analyses support the validity of predictions from basic crystal-chemistry considerations, as summarized in Table 3. In the approach [13,88,89], the preferential sites of substitution for Mn are determined by considering two parameters: (1) a ratio between the bond valence sums (BVS) [89] calculated for the Mn cations if placed on the Ca and Ti sites, respectively, of the actual $CaTiO_3$ structure and (2) a ratio of the Gold-

schmidt perovskite tolerance factors calculated for the hypothetical $MnTiO_3$ and $CaMnO_3$ structures (see Supplemental Information). If both ratios are less than unity, the Ca-site substitution is predicted, whereas in the opposite case, the Ti-site is considered favorable. The outcomes of this simplistic analysis match the thermodynamic predictions from the DFT modeling.

4. Summary and conclusions

In summary, the defect chemistry in the Mn-doped $CaTiO_3$ is shown to be influenced by octahedral rotations and the resulting structural distortions of the host structure. Consistent with basic crystal-chemistry considerations, Mn preferentially substitutes Ca on cuboctahedral sites as Mn^{2+}. Octahedral rotations accommodate the already small ion-size difference between Ca^{2+} and Mn^{2+} without any significant off-center displacements of the Mn ions. Concurrent substitution of Mn^{4+} for Ti^{4+} was also confirmed at concentrations lower than the $Mn_{Ca}^{\times}$ defect centers. The presence of both Mn^{2+} and Mn^{4+} on the Ca- and Ti-sites, respectively, was corroborated by both multi-frequency EPR and X-ray absorption fine structure measurements. First principles calculations using DFT supported the experimental results, providing insight into the structural mechanisms that facilitate the accommodation of Mn on the cuboctahedral sites in $CaTiO_3$. The DFT-based thermodynamic analyses rationalized the differences in the point-defect populations generated by the Mn substitution into $CaTiO_3$, $SrTiO_3$, and $BaTiO_3$, which can be readily explained in terms of basic crystal chemistry and the distortions of the host structures. Importantly, these analyses demonstrated that the formation of defect complexes between Ti-substituted Mn^{2+} ions and nearest-neighbor oxygen vacancies in $CaTiO_3$ are thermodynamically unstable under typical processing conditions, in contrast to observations in Mn-doped $SrTiO_3$ and $BaTiO_3$. Given that such defect complexes in perovskites have a strong impact on the mobility of oxygen vacancies [20,21], the incorporation of $CaTiO_3$ as a component in solid solutions (or using other means to induce/modify octahedral rotations) should be explored as a mechanism for tuning the mixed electronic/ionic-transport properties of perovskite formulations.

Declaration of Competing Interest

The authors declare that they have no known competing financial interests or personal relationships that could have appeared to influence the work reported in this paper.

Acknowledgments

The high-field EPR spectra were recorded at the NHMFL, which is funded by the NSF through the Cooperative Agreement No. DMR-1644779 and the State of Florida. A portion of this work was carried out with the support of the Diamond Light Source (beam time proposal SP16478).

Dr. Donohue acknowledges support under the Cooperative Research Agreement between the University of Maryland and the National Institute of Standards and Technology Center for Nanoscale Science and Technology, Award 70NANB10H193, through the University of Maryland.

Supplementary materials

Supplementary material associated with this article can be found, in the online version, at doi:10.1016/j.actamat.2021.116688.

References

[1] A.S. Bhalla, R. Guo, R. Roy, The perovskite structure - a review of its role in ceramic science and technology, Mater. Res. Innov. 4 (2000) 3–26, doi:10.1007/s100190000062.

[2] G. Brennecka, R. Sherbondy, R. Schwartz, J. Ihlefeld, Ferroelectricity-A revolutionary century of discovery, Am. Ceram. Soc. Bull. 99 (2020) 24–30.

[3] L.E. Cross, R.E. Newnham, History of Ferroelectrics, Ceram. Civiliz. III (1987) 289–305.

[4] F. Li, D. Lin, Z. Chen, Z. Cheng, J. Wang, C. Li, Z. Xu, Q. Huang, X. Liao, L.-.Q. Chen, T.R. Shrout, S. Zhang, Ultrahigh piezoelectricity in ferroelectric ceramics by design, Nat. Mater. 17 (2018) 349–354, doi:10.1038/s41563-018-0034-4.

[5] D. Damjanovic, Ferroelectric, dielectric and piezoelectric properties of ferroelectric thin films and ceramics, Reports Prog. Phys. 61 (1998) 1267–1324, doi:10.1088/0034-4885/61/9/002.

[6] P. Muralt, R.G. Polcawich, S. Trolier-McKinstry, Piezoelectric thin films for sensors, actuators, and energy harvesting, MRS Bull. 34 (2009) 658–664, doi:10.1557/mrs2009.177.

[7] C.A. Randall, R. Maier, W. Qu, K. Kobayashi, K. Morita, Y. Mizuno, N. Inoue, T. Oguni, Improved reliability predictions in high permittivity dielectric oxide capacitors under high dc electric fields with oxygen vacancy induced electromigration, J. Appl. Phys. 113 (2013) 014101, doi:10.1063/1.4772599.

[8] S. Rodewald, J. Fleig, J. Maier, Measurement of conductivity profiles in acceptor-doped strontium titanate, J. Eur. Ceram. Soc. 19 (1999) 797–801, doi:10.1016/s0955-2219(98)00317-3.

[9] J. Maier, Mass transport in the presence of internal defect reactions, J. Am. Ceram. Soc. 76 (1993) 1223–1227.

[10] R.A. De Souza, V. Metlenko, D. Park, T.E. Weirich, Behavior of oxygen vacancies in single-crystal $SrTiO_3$: equilibrium distribution and diffusion kinetics, Phys. Rev. B - Condens. Matter Mater. Phys. 85 (2012) 1–11, doi:10.1103/PhysRevB.85.174109.

[11] M. Kessel, R.A. De Souza, M. Martin, Oxygen diffusion in single crystal barium titanate, Phys. Chem. Chem. Phys. 17 (2015) 12587–12597, doi:10.1039/C5CP01187F.

[12] K. Shibuya, R. Dittmann, S. Mi, R. Waser, Impact of defect distribution on resistive switching characteristics of Sr_2TiO_4 thin films, Adv. Mater. 22 (2010) 411–414, doi:10.1002/adma.200901493.

[13] V.M. Goldschmidt, Crystal structure and chemical constitution, Trans. Faraday Soc. 25 (1929) 253, doi:10.1039/tf9292500253.

[14] I.M. Reaney, E.L. Colla, N. Setter, Dielectric and structural characteristics of Ba- and Sr-based complex perovskites as a function of tolerance factor, Jpn. J. Appl. Phys. 33 (1994) 3984–3990, doi:10.1143/JJAP.33.3984.

[15] A.T. Mulder, N.A. Benedek, J.M. Rondinelli, C.J. Fennie, Turning ABO_3 antiferroelectrics into ferroelectrics: design rules for practical rotation-driven ferroelectricity in double perovskites and $A_3B_2O_7$ ruddlesden-popper compounds, Adv. Funct. Mater. 23 (2013) n/a-n/a, doi:10.1002/adfm.201300210.

[16] C.J. Bartel, C. Sutton, B.R. Goldsmith, R. Ouyang, C.B. Musgrave, L.M. Ghiringhelli, M. Scheffler, New tolerance factor to predict the stability of perovskite oxides and halides, Sci. Adv. 5 (2019) eaav0693, doi:10.1126/sciadv.aav0693.

[17] C. Li, X. Lu, W. Ding, L. Feng, Y. Gao, Z. Guo, Formability of ABX_3 (X = F, Cl, Br, I) halide perovskites, Acta Crystallogr. Sect. B Struct. Sci. 64 (2008) 702–707, doi:10.1107/S0108768108032734.

[18] E.L. Colla, I.M. Reaney, N. Setter, Effect of structural changes in complex perovskites on the temperature coefficient of the relative permittivity, J. Appl. Phys. 74 (1993) 3414–3425, doi:10.1063/1.354569.

[19] R.E. Eitel, C.A. Randall, T.R. Shrout, P.W. Rehrig, W. Hackenberger, S.-.E. Park, New high temperature morphotropic phase boundary piezoelectrics based on $Bi(Me)O_3$–$PbTiO_3$ ceramics, Jpn. J. Appl. Phys. 40 (2001) 5999–6002, doi:10.1143/JJAP.40.5999.

[20] R.A. Maier, C.A. Randall, Low temperature ionic conductivity of an acceptor-doped perovskite: II. Impedance of single-crystal $BaTiO_3$, J. Am. Ceram. Soc. 99 (2016) 3360–3366, doi:10.1111/jace.14347.

[21] R.A. Maier, C.A. Randall, Low-temperature ionic conductivity of an acceptor-doped perovskite: I. Impedance of single-crystal $SrTiO_3$, J. Am. Ceram. Soc. 99 (2016) 3350–3359, doi:10.1111/jace.14348.

[22] R.A. Maier, A.C. Johnston-Peck, M.P. Donohue, (Magic Dopant) amphoteric behavior of a redox-active transition metal ion in a perovskite lattice: new insights on the lattice site occupation of manganese in $SrTiO_3$, Adv. Funct. Mater. 26 (2016) 8325–8333, doi:10.1002/adfm.201602156.

[23] K. Müller, T. Kool (Eds.), Properties of Perovskites and Other Oxides, World Scientific, Hackensack, NJ, 2010.

[24] D.J. Keeble, Z. Li, M. Harmatz, Electron paramagnetic resonance of Cu^{2+} in $PbTiO_3$, J. Phys. Chem. Solids. 57 (1996) 1513–1515, doi:10.1016/0022-3697(96)00021-2.

[25] D.J. Keeble, M. Loyo-Menoyo, Z.I.Y. Booq, R.R. Garipov, V.V. Eremkin, V. Smotrakov, Fe^{3+} defect dipole centers in ferroelectric $PbTiO_3$ studied using electron paramagnetic resonance, Phys. Rev. B. 80 (2009) 014101, doi:10.1103/PhysRevB.80.014101.

[26] U. Balachandran, N.G. Eror, Electrical conductivity in calcium titanate with excess CaO, Mater. Sci. Eng. 54 (1982) 221–228, doi:10.1016/0025-5416(82)90116-1.

[27] U. Balachandran, B. Odekirk, N.G. Eror, Electrical conductivity in calcium titanate, Mater. Sci. Eng. 54 (1982) 221–228, doi:10.1016/0025-5416(82)90116-1.

[28] U. Balachandran, N.G. Eror, On the defect structure of strontium titanate with excess SrO, J. Mater. Sci. 17 (1982) 2133–2140, doi:10.1007/BF00540432.

[29] U. Balachandran, B. Odekirk, N.G. Eror, Defect structure of acceptor-doped calcium titanate at elevated temperatures, J. Mater. Sci. 17 (1982) 1656–1662, doi:10.1007/BF00540792.

[30] T. Bak, J. Nowotny, C.C. Sorrell, M.F. Zhou, E.R. Vance, Charge transport in $CaTiO_3$: I. Electrical conductivity, J. Mater. Sci. Mater. Electron. 15 (2004) 635–644, doi:10.1023/B:JMSE.0000038917.73334.92.

[31] T. Bak, J. Nowotny, C.C. Sorrell, M.F. Zhou, Charge transport in $CaTiO_3$: II. Thermoelectric power, J. Mater. Sci Mater Electonics. 15 (2004) 645–650, doi:10.1023/B:JMSE.0000038918.70106.26.

[32] T. Bak, J. Nowotny, C.C. Sorrell, M.F. Zhou, Charge transport in $CaTiO_3$: III. Electrical conductivity, J. Mater. Sci. 15 (2004) 635–644, doi:10.1023/B:JMSE.0000038917.73334.92.

[33] M.F. Zhou, T. Bak, J. Nowotny, M. Rekas, C.C. Sorrell, E.R. Vance, Defect chemistry and semiconducting properties of calcium titanate, J. Mater. Sci. Mater. Electron. 13 (2002) 697–704, doi:10.1023/A:1021552602704.

[34] N. Abhyankar, A. Agrawal, P. Shrestha, R. Maier, R.D. McMichael, J. Campbell, V. Szalai, Scalable microresonators for room-temperature detection of electron spin resonance from dilute, sub-nanoliter volume solids, Sci. Adv. 6 (2020) eabb0620, doi:10.1126/sciadv.abb0620.

[35] a.M. Glazer, The classification of tilted octahedra in perovskites, Acta Crystallogr. Sect. B Struct. Crystallogr. Cryst. Chem. 28 (1972) 3384–3392, doi:10.1107/S0567740872007976.

[36] S. Lee, W.H. Woodford, C.a. Randall, Crystal and defect chemistry influences on band gap trends in alkaline earth perovskites, Appl. Phys. Lett. 92 (2008) 201909, doi:10.1063/1.2936091.

[37] P. Wise, I. Reaney, W. Lee, T. Price, D. Iddles, D. Cannell, Structure–microwave property relations in $(Sr_xCa_{(1-x)})_{n+1}Ti_nO_{3n+1}$, J. Eur. Ceram. Soc. 21 (2001) 1723–1726, doi:10.1016/S0955-2219(01)00102-9.

[38] N. Kumar, E.A. Patterson, T. Frömling, D.P. Cann, DC-bias dependent impedance spectroscopy of $BaTiO_3$–$Bi(Zn_{1/2}Ti_{1/2})O_3$ ceramics, J. Mater. Chem. C. 4 (2016) 1782–1786, doi:10.1039/C5TC04247J.

[39] J. Balachandran, L. Lin, J.S. Anchell, C.A. Bridges, P. Ganesh, Defect genome of cubic perovskites for fuel cell applications, J. Phys. Chem. C. 121 (2017) 26637–26647, doi:10.1021/acs.jpcc.7b08716.

[40] I. Levin, V. Krayzman, J.C. Woicik, A. Tkach, P.M. Vilarinho, X-ray absorption fine structure studies of Mn coordination in doped perovskite $SrTiO_3$, Appl. Phys. Lett. 96 (2010) 052904, doi:10.1063/1.3298369.

[41] V.V. Laguta, I.V. Kondakova, I.P. Bykov, M.D. Glinchuk, A. Tkach, P.M. Vilarinho, L. Jastrabik, Electron spin resonance investigation of Mn^{2+} ions and their dynamics in Mn-doped $SrTiO_3$, Phys. Rev. B. 76 (2007) 2–7, doi:10.1103/PhysRevB.76.054104.

[42] R.A. Maier, E. Cockayne, M. Donohue, G. Cibin, I. Levin, Substitutional mechanisms and structural relaxations for manganese in $SrTiO_3$: bridging the concentration gap for point-defect metrology, Chem. Mater. 32 (2020) 4651–4662, doi:10.1021/acs.chemmater.0c01082.

[43] B. Ravel, M. Newville, ARTEMIS ATHENA, HEPHAESTUS: data analysis for X-ray absorption spectroscopy using IFEFFIT, in: J. Synchrotron Radiat., International Union of Crystallography, 2005, pp. 537–541, doi:10.1107/S0909049505012719.

[44] J.J. Rehr, J.J. Kas, M.P. Prange, A.P. Sorini, Y. Takimoto, F. Vila, Ab initio theory and calculations of X-ray spectra, Comptes Rendus Phys 10 (2009) 548–559, doi:10.1016/j.crhy.2008.08.004.

[45] O. Bunău, Y. Joly, Self-consistent aspects of x-ray absorption calculations, J. Phys. Condens. Matter. 21 (2009) 345501, doi:10.1088/0953-8984/21/34/345501.

[46] W. Kohn, L.J. Sham, Self-consistent equations including exchange and correlation effects, Phys. Rev. 140 (1965) A1133–A1138, doi:10.1103/PhysRev.140.A1133.

[47] P. Giannozzi, S. Baroni, N. Bonini, M. Calandra, R. Car, C. Cavazzoni, D. Ceresoli, G.L. Chiarotti, M. Cococcioni, I. Dabo, A. Dal Corso, S. de Gironcoli, S. Fabris, G. Fratesi, R. Gebauer, U. Gerstmann, C. Gougoussis, A. Kokalj, M. Lazzeri, L. Martin-Samos, N. Marzari, F. Mauri, R. Mazzarello, S. Paolini, A. Pasquarello, L. Paulatto, C. Sbraccia, S. Scandolo, G. Sclauzero, A.P. Seitsonen, A. Smogunov, P. Umari, R.M. Wentzcovitch, QUANTUM ESPRESSO: a modular and open-source software project for quantum simulations of materials, J. Phys. Condens. Matter. 21 (2009) 395502, doi:10.1088/0953-8984/21/39/395502.

[48] D. Vanderbilt, Soft self-consistent pseudopotentials in a generalized eigenvalue formalism, Phys. Rev. B. 41 (1990) 7892–7895, doi:10.1103/PhysRevB.41.7892.

[49] J.P. Perdew, A. Ruzsinszky, G.I. Csonka, O.A. Vydrov, G.E. Scuseria, L.A. Constantin, X. Zhou, K. Burke, Restoring the density-gradient expansion for exchange in solids and surfaces, Phys. Rev. Lett. 100 (2008) 136406, doi:10.1103/PhysRevLett.100.136406.

[50] S.L. Dudarev, G.A. Botton, S.Y. Savrasov, C.J. Humphreys, A.P. Sutton, Electron-energy-loss spectra and the structural stability of nickel oxide: an LSDA+U study, Phys. Rev. B. 57 (1998) 1505–1509, doi:10.1103/PhysRevB.57.1505.

[51] R. Fletcher, Practical Methods of Optimization, 2nd Edition, John Wiley & Sons, Inc., New York, 1987.

[52] R.D. Shannon, C.T. Prewitt, Effective ionic radii in oxides and fluorides, Acta Crystallogr. Sect. B Struct. Crystallogr. Cryst. Chem. 25 (1969) 925–946, doi:10.1107/S0567740869003220.

[53] F.A. Kröger, H.J. Vink, Relations between the concentrations of imperfections in crystalline solids, in: Solid State Phys., 1956, pp. 307–435, doi:10.1016/S0081-1947(08)60135-6.

[54] J.S. Thorp, A.R. Skinner, The dependence of EPR linewidth on concentration in Mn/MgO single crystals, J. Magn. Magn. Mater. 69 (1987) 34–42, doi:10.1016/0304-8853(87)90209-5.

[55] C.P. Poole, H.A. Farach, Line shapes in electron spin resonance spectra, Bull. Magn. Reson. 1 (1979) 162–194 http://citeseerx.ist.psu.edu/viewdoc/download?doi=10.1.1.173.1067&rep=rep1&type=pdf. (accessed November 22, 2017).

[56] S. Stoll, A. Schweiger, EasySpin, a comprehensive software package for spectral simulation and analysis in EPR, J. Magn. Reson. 178 (2006) 42–55, doi:10.1016/j.jmr.2005.08.013.

[57] O. Stetsiuk, N. Plyuta, N. Avarvari, E. Goreshnik, V. Kokozay, S. Petrusenko, A. Ozarowski, Mn(III) chain coordination polymers assembled by Salicylidene-2-ethanolamine schiff base ligands: synthesis, crystal structures, and HFEPR study, Cryst. Growth Des. 20 (2020) 1491–1502, doi:10.1021/acs.cgd.9b01150.

[58] D.V. Azamat, A.G. Badalyan, A. Dejneka, V.A. Trepakov, L. Jastrabik, Z. Frait, High-frequency electron paramagnetic resonance investigation of Mn^{3+} centers in $SrTiO_3$, J. Phys. Chem. Solids. 73 (2012) 822–826, doi:10.1016/j.jpcs.2012.02.009.

[59] C.P. Poole, H.A. Farach, W.K. Jackson, Standardization of convention for zero field splitting parameters, J. Chem. Phys. 61 (1974) 2220–2221, doi:10.1063/1.1682294.

[60] C. Rudowicz, R. Bramley, On standardization of the spin Hamiltonian and the ligand field Hamiltonian for orthorhombic symmetry, J. Chem. Phys. 83 (1985) 5192–5197, doi:10.1063/1.449731.

[61] K.A. Müller, Electron paramagnetic resonance of manganese IV in $SrTiO_3$, Phys. Rev. Lett. 2 (1959) 341–343, doi:10.1103/PhysRevLett.2.341.

[62] D.J. Newman, B. Ng, The superposition model of crystal fields, Reports Prog. Phys. 52 (1989) 699–762, doi:10.1088/0034-4885/52/6/002.

[63] D.J. Newman, W. Urban, Interpretation of S state ion EPR spectra, Adv. Phys. 24 (1975) 793–844.

[64] D.J. Newman, The theory of lanthanide crystal fields, Adv. Phys. 20 (1971) 197–256.

[65] E. Šimánek, K.A. Müller, Covalency and hyperfine structure constant A of iron group impurities in crystals, J. Phys. Chem. Solids. 31 (1970) 1027–1040, doi:10.1016/0022-3697(70)90313-6.

[66] C. Rudowicz, P. Budzyński, P. Budzynski, Electron magnetic resonance studies of Fe^{3+} Ions in $BaTiO_3$: implications of the misinterpretation of zero-field splitting terms and comparative data analysis, Phys. Rev. B. 74 (2006) 054415, doi:10.1103/PhysRevB.74.054415.

[67] M. Açıkgöz, P. Gnutek, C. Rudowicz, Modeling zero-field splitting parameters for dopant Mn^{2+} and Fe^{3+} ions in anatase TiO_2 crystal using superposition model analysis, Chem. Phys. Lett. 524 (2012) 49–55, doi:10.1016/j.cplett.2011.12.042.

[68] P. Gnutek, M. Açıkgöz, C. Rudowicz, Superposition model analysis of the zero-field splitting parameters of Fe^{3+} doped in $TlInS_2$ crystal – Low symmetry aspects, Opt. Mater. (Amst). 32 (2010) 1161–1169, doi:10.1016/j.optmat.2010.03.024.

[69] P. Gnutek, C. Rudowicz, Diagonalization of second-rank crystal field terms for $3d^N$ and $4f^N$ ions at triclinic or monoclinic symmetry sites – case study: Cr^{4+} in Li_2MgSiO_4 and Nd^{3+} in β-BaB_2O_4, Opt. Mater. (Amst). 31 (2008) 391–400, doi:10.1016/j.optmat.2008.05.013.

[70] W.G. Waller, M.T. Rogers, A generalization of methods for determining g tensors, J. Magn. Reson. 9 (1973) 92–107, doi:10.1016/0022-2364(73)90164-9.

[71] A. Lund, T. Vänngård, Note on the determination of the principal fine and hyperfine coupling constants in ESR, J. Chem. Phys. 42 (1965) 2979–2980, doi:10.1063/1.1703280.

[72] C. Rudowicz, Relations between arbitrary symmetry spin-hamiltonian parameters Bkq and bkq in various axis systems, J. Magn. Reson. 63 (1985) 95–106, doi:10.1016/0022-2364(85)90156-8.

[73] C. Rudowicz, S.B. Madhu, I. Akhmadoulline, COMPARE: a computer program for comparative analysis of EPR data for low-symmetry paramagnetic centers, Appl. Magn. Reson. 16 (1999) 447–456, doi:10.1007/BF03161941.

[74] H. Matsuoka, K. Furukawa, K. Sato, D. Shiomi, Y. Kojima, K. Hirotsu, N. Furuno, T. Kato, T. Takui, Importance of fourth-order zero-field splitting terms in random-orientation EPR spectra of Eu(II)-doped strontium aluminate, J. Phys. Chem. A. 107 (2003) 11539–11546, doi:10.1021/jp030819+.

[75] E. Siegel, K.A. Müller, Structure of transition-metal—Oxygen-vacancy pair centers, Phys. Rev. B. 19 (1979) 109–120, doi:10.1103/PhysRevB.19.109.

[76] K.A. Müller, W. Berlinger, K.W. Blazey, J. Albers, Electron paramagnetic resonance of Mn^{4+} in $BaTiO_3$, Solid State Commun 61 (1987) 21–25, doi:10.1016/0038-1098(87)90007-X.

[77] D.J. Keeble, Z. Li, E.H. Poindexter, Electron paramagnetic resonance of Mn^{4+} in $PbTiO_3$, J. Phys. Condens. Matter. 7 (1995) 6327–6333, doi:10.1088/0953-8984/7/31/015.

[78] Yu Wan-Lun, Zhao Min-Guang, Spin-Hamiltonian parameters of ^{6}S-state ions, Phys. Rev. B. 37 (1988) 9254–9267, doi:10.1103/PhysRevB.37.9254.

[79] E. Siegel, K.A. Muller, Local position of Fe^{3+} in ferroelectric $BaTiO_3$, Phys. Rev. B. 20 (1979) 3587–3596.

[80] P. Gnutek, Z.Y. Yang, C. Rudowicz, Modeling local structure using crystal field and spin Hamiltonian parameters: the tetragonal Fe_K^{3+}-O_I^{2-} defect center in $KTaO_3$ crystal, J. Phys. Condens. Matter. 21 (2009), doi:10.1088/0953-8984/21/45/455402.

[81] J. Rubio O., H. Murrieta S., G. Aguilar S., Superposition model analysis of the cubic spin-Hamiltonian parameters for Mn^{2+} and Fe^{3+} in the alkaline earth oxides, fluoroperovskite, and II–VI compounds, J. Chem. Phys. 71 (1979) 4112–4122, doi:10.1063/1.438182.

[82] A. Manceau, M.A. Marcus, S. Grangeon, Determination of Mn valence states in mixed-valent manganates by XANES spectroscopy, Am. Mineral. 97 (2012) 816–827, doi:10.2138/am.2012.3903.

[83] K. Reuter, M. Scheffler, Composition, structure, and stability of RuO_2 (110) as a function of oxygen pressu, Phys. Rev. B. 65 (2001) 035406, doi:10.1103/PhysRevB.65.035406.

[84] R.A. Maier, T.A. Pomorski, P.M. Lenahan, C.A. Randall, Acceptor-oxygen vacancy defect dipoles and fully coordinated defect centers in a ferroelectric perovskite lattice : electron paramagnetic resonance analysis of Mn^{2+} in single crystal $BaTiO_3$, J. Appl. Phys. 118 (2015) 164102, doi:10.1063/1.4934505.

[85] I. Kondakova, R. Kuzian, L. Raymond, R. Hayn, V. Laguta, Evidence for impurity-induced polar state in $Sr_{1-x}Mn_xTiO_3$ from density functional calculations, Phys. Rev. B. 79 (2009) 1–7, doi:10.1103/PhysRevB.79.134117.
[86] K.W. Blazey, J.M. Cabrera, K.A. Müller, Oxygen vacancy-transition metal-ion impurity association in $SrTiO_3$, Solid State Commun 45 (1983) 903–906, doi:10.1016/0038-1098(83)90332-0.
[87] R.A. Serway, W. Berlinger, K.A. Muller, R.W. Collins, Electron-paramagnetic resonance of 3 manganese centers in reduced $SrTiO_3$, Phys. Rev. B. 16 (1977) 4761–4768, doi:10.1103/PhysRevB.16.4761.
[88] I.D. Brown, Influence of chemical and spatial constraints on the structures of inorganic compounds, Acta. Cryst. B53 (1997) 381–393, doi:10.1107/S0108768197002474.
[89] I.D. Brown, Recent developments in the methods and applications of the bond valence model, Chem. Rev. 109 (2009) 6858–6919, doi:10.1021/cr900053k.